

Dynamical Control of Quantum Heat Engines Using Exceptional Points

J.-W. Zhang,^{1,2,*} J.-Q. Zhang,^{1,*} G.-Y. Ding,^{1,3,*} J.-C. Li,^{1,3} J.-T. Bu,^{1,3} B. Wang,^{1,3} L.-L. Yan,⁴
S.-L. Su,⁴ L. Chen,^{1,2} F. Nori,^{5,6} S. K. Özdemir,⁷ F. Zhou,^{1,2,†} H. Jing,^{8,9,‡} and M. Feng^{1,2,4,§}

¹*State Key Laboratory of Magnetic Resonance and Atomic and Molecular Physics, Wuhan Institute of Physics and Mathematics, Innovation Academy of Precision Measurement Science and Technology, Chinese Academy of Sciences, Wuhan, 430071, China*

²*Research Center for Quantum Precision Measurement, Guangzhou Institute of Industry Technology, Guangzhou, 511458, China*

³*School of Physics, University of the Chinese Academy of Sciences, Beijing 100049, China*

⁴*School of Physics, Zhengzhou University, Zhengzhou 450001, China*

⁵*Theoretical Quantum Physics Laboratory, RIKEN,*

Cluster for Pioneering Research, Wako-shi, Saitama 351-0198, Japan

⁶*Physics Department, The University of Michigan, Ann Arbor, Michigan 48109-1040, USA*

⁷*Department of Engineering Science and Mechanics, and Materials Research Institute, Pennsylvania State University, University Park, State College, Pennsylvania 16802, USA*

⁸*Key Laboratory of Low-Dimensional Quantum Structures and Quantum Control of Ministry of Education, Department of Physics and Synergetic Innovation Center for Quantum Effects and Applications, Hunan Normal University, Changsha 410081, China*

⁹*Synergetic Innovation Academy for Quantum Science and Technology, Zhengzhou University of Light Industry, Zhengzhou 450002, China*

(Dated: October 25, 2022)

A quantum thermal machine is an open quantum system coupled to hot and cold thermal baths. Thus, its dynamics can be well understood using the concepts and tools from non-Hermitian quantum systems. A hallmark of non-Hermiticity is the existence of exceptional points where the eigenvalues of a non-Hermitian Hamiltonian or an Liouvillian superoperator and their associated eigenvectors coalesce. Here, we report the experimental realisation of a single-ion heat engine and demonstrate the effect of the Liouvillian exceptional points on the dynamics and the performance of a quantum heat engine. Our experiments have revealed that operating the engine in the exact- and broken-phases, separated by a Liouvillian exceptional point, respectively during the isochoric heating and cooling strokes of an Otto cycle produces more work and output power and achieves higher efficiency than executing the Otto cycle completely in the exact phase where the system has an oscillatory dynamics and higher coherence. This result opens interesting possibilities for the control of quantum heat engines and will be of interest to other research areas that are concerned with the role of coherence and exceptional points in quantum processes and in work extraction by thermal machines.

Quantum heat engines extract useful work from thermal reservoirs using quantum matter as their working substance. Contrary to their classical counterparts, which do not include coherence in its microscopic degrees of freedom and suffer from irreversible loss during a classical thermodynamic cycle, quantum heat engines are expected to benefit from quantum features to surpass the output power and efficiency that can be attained by an equivalent classical heat engine [1–4]. The growing interest in quantum heat engines is also fueled by the interest in understanding the quantum-classical transition in energy-information and work-heat conversion. Additional motivations include the need to maximise the efficiency (the ratio of useful work to the input heat) and the output power while keeping power fluctuations minimal in micro- and nano-scale heat engines, in which quantum fluctuations and non-equilibrium dynamics play a crucial role [5–9]. Microscopic and nanoscopic heat engines with and without the involvement of quantum coherences

have been implemented with single trapped ions [8–10], ensembles of nitrogen-vacancy centres in diamond [4], magnetic resonance [11, 12], a single electron box [13], and impurity electron spins in a silicon tunnel field-effect transistor [14]. Many interesting proposals have also been put forward for their realisation in superconducting circuits [15, 16] and optomechanics [17, 18].

Another field that has been attracting increasing interest is non-Hermiticity, including parity-time (PT) symmetry [19] in physical systems. In particular, non-Hermitian spectral degeneracies known as exceptional points (EPs) have been shown to have tremendous effects on the dynamics of physical systems, leading to many counterintuitive features which have led to the development of novel functionalities and classical devices [20–27]. Effects of non-Hermiticity have generally been studied by an effective non-Hermitian Hamiltonian and its spectral degeneracies. Recently, there is a growing interest to harness non-Hermiticity and EPs for quantum applications [28–33]. In quantum systems, however,

Hamiltonian EPs (known as HEPs) cannot capture the whole dynamics because these exclude quantum jumps and the associated noises. Instead, one should resort to the Liouvillian formalism which takes into account both coherent non-unitary evolution and quantum jumps [3, 35–38]. In this formalism, EPs are defined as the degenerate eigenvalues of Liouvillian superoperators. Thus they are referred to Liouvillian EPs (LEPs), whose properties and effects on quantum systems have remained largely unexplored except in some recent experiments in superconducting qubit systems [38, 39].

As open quantum systems which exchange energy with thermal reservoirs, quantum heat engines naturally exhibit non-Hermitian dynamics, which can be controlled by judiciously tuning parameters of the heat engine to operate it in the exact- or broken-phases separated by LEPs (i.e., LEPs correspond to the transition points between the exact- to the broken- phases). Here we report the experimental implementation of a quantum Otto engine using a single $^{40}\text{Ca}^+$ ion confined in a linear Paul trap [2, 40, 42], and demonstrate the control of the engine efficiency and output power by harnessing LEPs and their associated dynamics. This constitutes an interesting observation of the signatures of LEPs in a quantum heat engine. We note that previous experiments studied non-Hermiticity in single-spin systems by considering only HEPs [28, 31, 32]. In contrast, here we use LEPs and their ramifications to control the performance of a quantum heat engine. Thus, our study takes into account quantum jumps and the associated dynamics. As it will become clear below and discussed in [37, 38], the LEP in this system corresponds to the critical damping point which emerges in the parameter space as the system transits between the oscillatory and non-oscillatory dynamics, in analogy with a damped harmonic oscillator.

Results

System of the single-ion quantum heat machine.

The working substance of the quantum Otto engine we implement here is a pseudo-spin $1/2$ represented by the internal states of a trapped single $^{40}\text{Ca}^+$ ion, i.e., a qubit encoded in the ground state $|4^2S_{1/2}, m_J = +1/2\rangle$ labeled as $|g\rangle$, and the metastable state $|3^2D_{5/2}, m_J = +5/2\rangle$ labeled as $|e\rangle$, with the magnetic quantum number m_J (see Fig. 1A). In our experiment, we confine a single $^{40}\text{Ca}^+$ ion in a linear Paul trap, whose axial and radial frequencies are $\omega_z/2\pi = 1.1$ MHz and $\omega_r/2\pi = 1.6$ MHz, respectively. We define a quantization axis along the axial direction by a magnetic field of approximately 3.4 Gauss at the center of the trap. We then perform Doppler and sideband cooling of the ion until an average phonon number of $\bar{n} < 1$ with the Lamb-Dicke parameter ~ 0.11 is achieved. This is sufficient to avoid thermal phonons yielding offsets of Rabi oscillations [2, 40, 42], and thus observe quantum

effects [42]. Populations of different energy levels of the qubit are detected using a photomultiplier tube (PMT) that monitors the fluorescence due to spontaneous decay from the excited state [2]. In our experiment, we observe the variation of the population in $|e\rangle$, from which the required thermodynamic quantities, such as work, output power and efficiency, can be acquired. The temperature T and the entropy S of a spin system are defined as $T = -\Delta_0[k_B \ln(P_e/P_g)]^{-1}$ and $S = -k_B \text{Tr}[\rho \ln \rho]$, where P_e and P_g denote the populations of the states $|e\rangle$ and $|g\rangle$, respectively, $\Delta_0 = E_e - E_g$ is the effective energy gap between the states $|e\rangle$ and $|g\rangle$ in the interaction representation, k_B is the Boltzmann constant, and ρ is the density operator describing the state of the system.

Under proper laser irradiation as in Fig. 1B, we obtain an effective two-level model with engineered drive and decay (Supplementary Note 1), as shown in Fig. 1C, which can be described by the Lindblad master equation,

$$\dot{\rho} = -i[H, \rho] + \frac{\gamma_{\text{eff}}}{2}(2\sigma_- \rho \sigma_+ - \sigma_+ \sigma_- \rho - \rho \sigma_+ \sigma_-) \equiv \mathcal{L}\rho, \quad (1)$$

where \mathcal{L} is the Liouvillian superoperator, ρ denotes the density operator, γ_{eff} is the effective decay rate from the excited state $|e\rangle$ to the ground state $|g\rangle$ (Supplementary Note 1), and

$$H = \Delta|e\rangle\langle e| + \frac{1}{2}\Omega(t)|e\rangle\langle g| + \text{H.c.}, \quad (2)$$

with Δ denoting the frequency detuning between the driving laser and the resonance transition of the ion and $\Omega(t)$ representing the drive amplitude (i.e., Rabi frequency) of the laser [2, 40, 42]. The dynamics of the system is fully captured by the Liouvillian superoperator \mathcal{L} whose eigenvalues for $\Delta = 0$ are $\lambda_1 = 0$, $\lambda_2 = -\gamma_{\text{eff}}$, $\lambda_3 = (-3\gamma_{\text{eff}} - \xi)/4$, and $\lambda_4 = (-3\gamma_{\text{eff}} + \xi)/4$, with $\xi = \sqrt{\gamma_{\text{eff}}^2 - 16\Omega^2}$ (Supplementary Note 2 and Supplementary Figure 1). When $\xi = 0$, that is $\gamma_{\text{eff}} = 4\Omega$, the eigenvalues λ_3 and λ_4 merge, giving rise to a second order LEP at $\lambda = -3\gamma_{\text{eff}}/4$. Clearly, for $\gamma_{\text{eff}} > 4\Omega$ (weak coupling), both λ_3 and λ_4 are real with a splitting amount ξ , corresponding to the broken phase characterised by a non-oscillatory dynamics with purely exponential decay [43, 44]. For $\gamma_{\text{eff}} < 4\Omega$ (strong coupling), on the other hand, λ_3 and λ_4 form a complex conjugate pair which splits in their imaginary parts by ξ , corresponding to the exact phase characterised by an oscillatory dynamics. Thus, the LEP divides the parameter space into a region of oscillatory dynamics (exact phase, $\gamma_{\text{eff}} < 4\Omega$) and a region of non-oscillatory dynamics (broken phase, $\gamma_{\text{eff}} > 4\Omega$). As such, the LEP here is similar to the critical damping point of a damped harmonic oscillator and emerges in the transition between the regions of oscillatory (exact phase) and non-oscillatory (broken phase) dynamics.

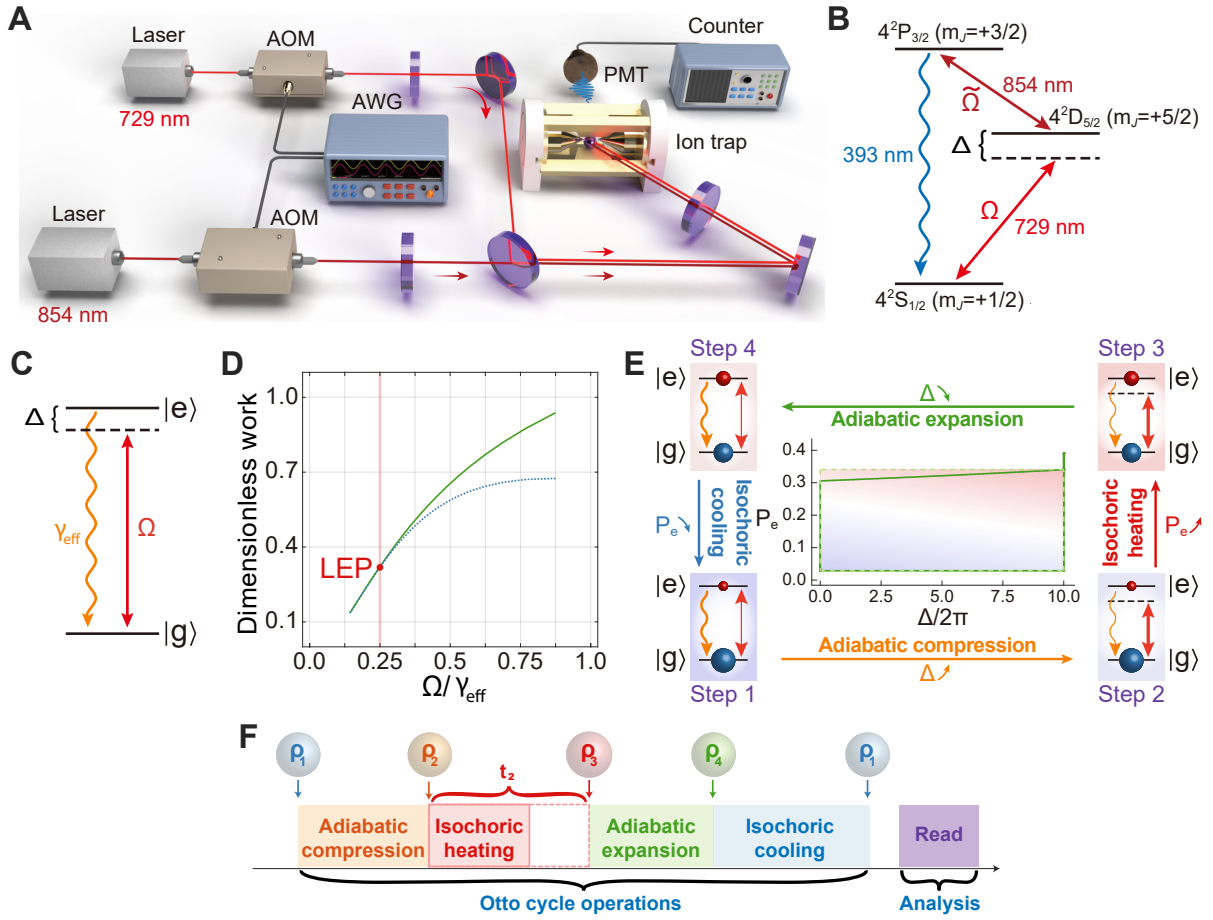


FIG. 1. **Single-spin quantum heat engine in a trapped $^{40}\text{Ca}^+$ ion exhibiting a Liouvillian exceptional point (LEP).** (A) Schematic of the experimental setup. AOM: acousto-optic modulator. PMT: photomultiplier tube. AWG: arbitrary waveform generator. (B) Energy levels of the $^{40}\text{Ca}^+$ ion, where the straight red arrows represent transitions by laser irradiation with wavelengths labeled and the blue wavy arrow denotes spontaneous emission. Such a three-level configuration equals an effective two-level system with controllable driving and decay, as plotted in (C). (D) Schematic diagram for work done in the exact- and broken-phases separated in the parameter space by an LEP at $\Omega/\gamma_{\text{eff}} = 1/4$, where a bifurcation occurs due to coherence-induced oscillations in the exact phase. (E) Four strokes of our quantum Otto engine, where strokes from Step 1 to Step 2 and from Step 3 to Step 4 are adiabatic processes; while strokes from Step 2 to Step 3 and from Step 4 to Step 1 represent isochoric processes. The green dashed line represents an ideal quantum Otto cycle, and the solid line corresponds to the cycle obtained by solving the master equation using experimentally available parameter values. (F) Experimental operation sequences for an Otto cycle, where the duration t_2 of the second stroke (isochoric heating) is varied to quantify the quantumness involved in the cycle.

Quantum Otto cycles of a single ion. The question we address in this study is: How do the presence of LEPs and the associated transitions between the oscillatory and non-oscillatory dynamics affect the performance of an Otto engine? A typical Otto cycle has four strokes: two adiabatic strokes, which result in compression and expansion, and two isochoric strokes which connect the working substance to cold and hot baths. Quantum Otto cycles differ from their classical counterparts in the varying and invariant thermodynamic quantities, and how these quantities are defined, see Supplementary Note 3 and Supplementary Figure 2. For example, in a quantum isochoric stroke, the population P_n of each level

n of the qubit, and hence the entropy S of the system, changes until the working substance reaches thermal equilibrium with the heat bath, while there is no change in the eigenenergies E_n [4, 5, 14].

In a classical isochoric process, the pressure P and the temperature T change but the volume V remains unchanged, and the working substance reaches thermal equilibrium with the heat bath only at the end of this process. In a classical adiabatic stroke, all thermodynamic quantities P , T , and the volume V vary (i.e., no invariant thermodynamic quantity) and there is no requirement that occupation probabilities remain unchanged. Therefore, work is done only during

the classical adiabatic strokes (no work is done during classical isochoric strokes). Similarly, a quantum heat engine does work only during the quantum adiabatic strokes (i.e., no work is done during the quantum isochoric strokes) but with a different underlying mechanism than the classical adiabatic strokes: In a quantum adiabatic stroke, P_n and S should remain unchanged during the process (thus no heat exchange) but E_n may shift. This change in E_n leads to non-zero work.

As demonstrated later, we find that the coherence-enabled improvements in work and power output of a quantum heat engine arise if the coherence during the work strokes (i.e., quantum adiabatic strokes) induces a hump in the thermal strokes (i.e., quantum isochoric strokes). Therefore, to answer the question stated above and clarify the relation among LEPs, the surviving coherence after the thermal strokes, and the performance of a quantum heat engine, we have designed experiments implementing Otto cycles with (i) both isochoric strokes in the exact phase ($\gamma_{\text{eff}} < 4\Omega$, oscillatory dynamics), (ii) both isochoric strokes in the broken phase ($\gamma_{\text{eff}} > 4\Omega$, non-oscillatory dynamics), and (iii) isochoric heating stroke in the exact but isochoric cooling stroke in the broken phases. We note that a fourth case would be the opposite of (iii), corresponding to a quantum refrigerator, totally reversing the process of the heat engine under the setting (iii). This case is beyond the scope of the present study and thus we have not performed experiments under this setting.

In our system of a single trapped ion, we implement the ingredients of the Otto cycle as follows: Hot and cold heat baths are prepared by tuning $\Omega/\gamma_{\text{eff}}$, which is the ratio of the driving laser beam strength Ω to the effective decay γ_{eff} of the qubit. This implies that laser irradiation together with the real environment constitutes the baths, where the hot and cold baths correspond to strong and weak drives, respectively. The qubit absorbs or releases heat by coupling to the hot or the cold baths, respectively. Here, we adjust γ_{eff} by varying the power of the laser with wavelength 854 nm, which is tuned to the $P_{3/2} - D_{5/2}$ transition and Ω is adjusted by tuning the power of the 729 nm laser red-tuned to the $S_{1/2} - D_{5/2}$ transition (Fig. 1B). We evaluate the performance of the heat engine, e.g., the work output to the cold bath and heat absorbed from the hot bath, by monitoring the variation in the populations of the two-level system.

In our treatment under the rotating frame with respect to the driving laser frequency, quantum adiabatic strokes are executed by tuning the frequency of the driving laser which helps vary the internal energy gap Δ (but without population change) and the temperature of the working substance. Similarly, quantum isochoric strokes are performed by tuning $\Omega/\gamma_{\text{eff}}$ which controls the heat exchange between the working substance and the thermal baths. Thus, while the power of the 854

nm laser helps tune the qubit decay, the power and the frequency of the 729 nm laser helps implement the four strokes of the Otto cycle as follows (Fig. 1E, F and Supplementary Figure 2): Starting with the qubit at steady state with a small population in the excited state, we first carry out an adiabatic compression by increasing the detuning Δ linearly from Δ_{min} to Δ_{max} , where P_e remains in a small and constant value (Step 1 \rightarrow Step 2). Next, we perform isochoric heating by rapidly increasing $\Omega/\gamma_{\text{eff}}$ to a large value, during which the detuning remains equal to Δ_{max} (Step 2 \rightarrow Step 3). Then, we carry out an adiabatic expansion by linearly decreasing Δ from Δ_{max} to Δ_{min} , with P_e staying unchanged (Step 3 \rightarrow Step 4). Finally, we perform isochoric cooling by rapidly decreasing $\Omega/\gamma_{\text{eff}}$ to a small value with the Δ remaining unchanged as Δ_{min} (Step 4 \rightarrow Step 1). To accomplish a closed Otto cycle, we wait, after finishing the last stroke, for the system reaching the steady state and returning to the initial state.

Performances of the single-ion quantum heat engine.

We evaluate the role of coherence in the performance of the quantum heat engine by monitoring the oscillations in the populations of the qubit states in the isochoric stroke and then assess the net work, the output power, and the efficiency of the heat engine as a function of the execution time t_2 of the second stroke (isochoric heating) while the execution times of other strokes are kept fixed (Supplementary Notes 4 and 5).

The strong coupling and the exact-phase regimes overlap for $\Omega/\gamma_{\text{eff}} > 1/4$ and similarly the weak coupling and the broken-phase regimes overlap for $\Omega/\gamma_{\text{eff}} < 1/4$, with the LEP at $\Omega/\gamma_{\text{eff}} = 1/4$ being the transition point. Our theoretical study and numerical simulations indicate that in the broken phase (weak coupling regime), the net work produced in an Otto cycle linearly increases with increasing $\Omega/\gamma_{\text{eff}}$. As $\Omega/\gamma_{\text{eff}}$ is increased to transit into the exact phase (strong coupling), the net work increases with $\Omega/\gamma_{\text{eff}}$ in a slower and bifurcated fashion due to enhancement of the coherence in the isochoric strokes, as shown in Fig. 1D. Therefore, as we will show below, by tuning $\Omega/\gamma_{\text{eff}}$, and hence the competition between the driving field strength and the qubit decay, one may elucidate the effects of LEPs, non-Hermiticity, and the associated changes in coherence on the net work, output power, and efficiency of the quantum heat engine.

First, we implement both of the isochoric strokes in the exact phase (i.e., the regime with complex conjugate eigenvalue pairs and hence with oscillatory dynamics). The time evolution of the excited state population P_e during the full Otto cycle exhibits a hump in the second stroke (i.e., isochoric heating) and a ramp in the fourth stroke (i.e., isochoric cooling), which reflect the sufficient coherence involved due to the strong coupling effect (Supplementary Note 4 and Supplementary Figure 4), in full agreement with the results obtained from the

simulations of the master equation (Fig. 2A₁). These features are also seen when the output power and the net amount of work are obtained as a function of the execution time t_2 of the second stroke, while the execution time of the other strokes are kept fixed (Fig. 2A₂). The clear hump at $t_2 \approx 4 \mu\text{s}$ is an indication of the role of coherence in the second stroke on the output power and the net work. We evaluate the efficiency of the Otto cycles in our experiments by calculating both the conventional efficiency η_c (defined as the ratio of the net work to the heat absorbed during a full Otto cycle) and the heat absorption efficiency η_q of the second stroke (i.e., quantum engine efficiency), which corresponds to the energy difference between the initial and end time points of the second stroke (Supplementary Note 3). We find that (Fig. 2A₃): (i) both η_c and η_q exhibit humps with a trend similar to that observed in the net work and output power plots, implying the involvement of coherence in the process, (ii) η_c is less than the efficiency $\eta_O = 1$ of the ideal Otto cycle, that is $\eta_c < \eta_O$, and (iii) $\eta_c < \eta_q$, indicating heat absorption during both the isochoric heating and the isochoric cooling strokes (2nd and 4th strokes).

Heat absorption during the isochoric cooling stroke is expected only in quantum systems and is a result of coherence (i.e., see the ramp in Fig. 2A₁). This additional heat absorption in the cooling stroke might be the reason for $\eta_c < \eta_O$, which suggests that for improved η_c , one should prevent heat absorption during the cooling stroke by minimising, if not removing, the coherence during this cycle. We note that there is a slight reduction in the population of the excited state $|e\rangle$ during the first and third strokes (Fig. 2A₁). This deviation from the ideal theoretical expectation (i.e., no population change during the adiabatic compression and expansion strokes) can be attributed to the fact that in the experiments the frequency of the 729 nm laser was not tuned smoothly in a continuous fashion but instead we used a sequence of discrete steps using an AOM (Supplementary Note 6). When this imperfection is taken into account, we observe a good agreement between theory and our experimental results. So the slight unexpected deviation in the excited state population does not affect our identification of the Otto cycle physics.

Next, we implement both of the isochoric strokes in the broken phase (i.e., the regime with real eigenvalues: non-oscillatory exponentially decaying dynamics). In contrast to the previous case, in which both isochoric strokes were implemented in the exact phase (oscillatory dynamics), the time evolution of the excited state population P_e in this case exhibits neither a hump nor a ramp during the isochoric strokes and P_e stays small during the full Otto cycle (Fig. 2B₁) due to weak coupling, in agreement with the results obtained by solving the Master equation. This indicates that coherence is largely erased during the isochoric strokes implemented in the broken phase, and

thus the net work and output power are much smaller (Fig. 2B₂). In this regime, we observe that η_c stays almost constant and has a value very close to η_O as t_2 is varied, whereas η_q gradually increases and attains a value very close to η_O after $t_2 = 4 \mu\text{s}$ (Fig. 2A₃), indicating that the net work is nearly equivalent to the heat absorbed during the isochoric heating (i.e., 2nd stroke). This is a typical feature of classical Otto cycles, where quantum coherence is not involved.

We note that due to the cold reservoir at the effective temperature $T = 0$ K with $\Delta = 0$, the Otto cycle efficiency η_c we observe here is $\eta_c \simeq 99.07\%$, which is much higher than the efficiencies reported previously for heat engines implemented in a ^{13}C nucleus [12], a trapped ion [10], and a quantum dot [47]. Moreover, comparison of the different conditions in Figs. 2 and 3 suggests that larger reduction in coherence during an Otto cycle, by executing the isochoric strokes in the broken phase, results in higher η_c , but significantly reduced net work and output power.

The two sets of experiments discussed above suggest that coherence in the isochoric heating and cooling strokes of the Otto cycle enhances the net work and output power at the expense of the efficiency η_c , which approaches the ideal value when coherence involved during the isochoric strokes is not sufficient. These experiments also suggest that coherence-enabled heat absorption during the isochoric cooling cycle is the reason for the reduced η_c , when isochoric strokes are implemented in the exact phase (Supplementary Figure 4).

These results open a window of opportunity to achieve high η_c simultaneously with high net work and output power: Execute the isochoric heating in the exact phase, but the isochoric cooling in the broken phase. Implementing the isochoric cooling in the broken phase will largely reduce the coherence and thus significantly decrease the amount of heat absorption during the cooling stroke. This will prevent the reduction in η_c and at the same time generates more work and power. In order to confirm this prediction, we have designed the final experiments in such a way that the isochoric heating is executed in the exact phase, whereas the isochoric cooling is executed in the broken phase. The time evolution of the excited state population P_e in this case exhibits a hump during the heating stroke which is executed in the exact phase and no ramp is seen during the cooling stroke, which is executed in the broken phase (Fig. 3A). This implies the existence of sufficient coherence only during the heating stroke but not during the cooling stroke. The maximum value of P_e is as high as the value obtained for the case when both isochoric strokes are executed in the exact phase. The hump (which is the signature of the presence of sufficient coherence) is seen in the plots of: net work, output power, η_q versus t_2 , and η_c versus t_2 (Fig. 3B, C). The

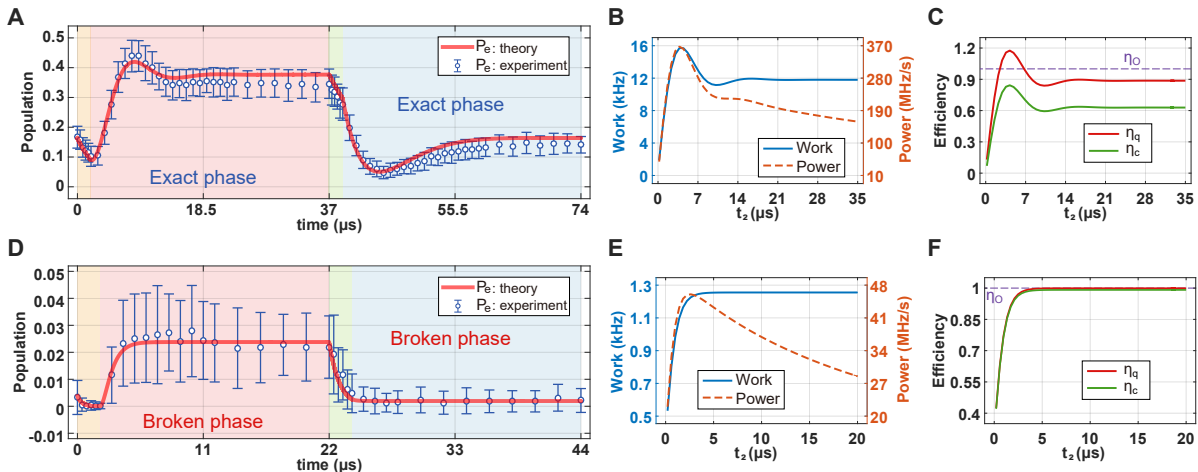


FIG. 2. **Otto cycles with the isochoric processes executed in the exact- or the broken-phase.** (A₁) and (B₁), Time evolution of the population in the excited state $|e\rangle$ when both the second (isochoric heating) and the fourth (isochoric cooling) strokes are in the exact (strong drive and oscillatory dynamics)- and broken (weak drive and non-oscillatory dynamics) phases, respectively. The red solid curves are obtained by simulating the master equation. The circles and the error bars, respectively, denote the average and standard deviation of 10,000 measurements. Regions with different colors correspond to different strokes of the Otto cycle, with the orange, pink, green, and blue corresponding to the first (adiabatic compression), second (isochoric heating), third (adiabatic expansion), and fourth (isochoric cooling) strokes, respectively. The first (orange) and the third (green) strokes are implemented by up- and down-scanning the detuning Δ between $\Delta_{\min}/2\pi = 0$ kHz, and $\Delta_{\max}/2\pi = 10$ kHz, respectively, with constant Ω and γ_{eff} . The second (pink) and the fourth (blue) strokes are implemented by rapidly increasing and decreasing $\Omega/\gamma_{\text{eff}}$ with constant detuning. In (A₁), we used $\{\Omega/2\pi = 23$ kHz, $\gamma_{\text{eff}} = 300$ kHz $\}$, and $\{\Omega/2\pi = 24$ kHz, $\gamma_{\text{eff}} = 120$ kHz $\}$ for the first and third strokes, respectively, and $\{\Omega/2\pi = 82$ kHz, $\gamma_{\text{eff}} = 370$ kHz, $\Delta = \Delta_{\max}\}$ and $\{\Omega/2\pi = 24$ kHz, $\gamma_{\text{eff}} = 299$ kHz, $\Delta = \Delta_{\min}\}$ for the second and fourth strokes. In (B₁), we used $\{\Omega/2\pi = 25$ kHz, $\gamma_{\text{eff}} = 2500$ kHz $\}$ and $\{\Omega/2\pi = 25$ kHz, $\gamma_{\text{eff}} = 970$ kHz $\}$ for the first and third strokes, respectively, and $\{\Omega/2\pi = 64$ kHz, $\gamma_{\text{eff}} = 2500$ kHz, $\Delta = \Delta_{\max}\}$ and $\{\Omega/2\pi = 25$ kHz, $\gamma_{\text{eff}} = 2500$ kHz, $\Delta = \Delta_{\min}\}$ for the second and fourth strokes. (A₂) and (B₂), The net work and output power, and (A₃) and (B₃), the efficiencies η_c and η_q as functions of the second stroke execution time t_2 while the execution times of the other strokes are kept fixed. In (A₃) and (B₃), the horizontal dashed lines represent the efficiency $\eta_0 = 1$ of the ideal Otto cycle.

net work and the output power obtained in this setting (Fig. 3B) are much higher than the previous two settings, whose results are given in Fig. 2A₂ and 2B₂. Moreover, we obtain $\eta_c \approx 1$ for $t_2 \leq 5$ μs , implying that the net work is nearly equivalent to the absorbed heat during the heating stroke. This is the result of the absence of sufficient coherence and hence less heat absorption during the cooling stroke.

Note that η_c experiences only a very small decrease down to $\eta_c \approx 0.9$ for longer t_2 , which is much higher than the $\eta_c \sim 0.65$ obtained when both isochoric strokes are executed in the exact phase, and only slightly lower than the $\eta_c = 1$ obtained when both strokes are executed in the broken phase. We note that the net work, output power, η_c , and η_q achieved their maximum at $t_2 = 4$ μs . Our experiments clearly demonstrate that the exact phase (and hence more coherence) during the isochoric heating (second stroke) and broken phase (and hence less coherence) during the isochoric cooling (fourth stroke) lead to a better quantum heat engine performance.

Discussion

We have implemented a quantum heat engine using a

single trapped ion and elucidated the role of coherence, LEPs, and the associated dynamics in the performance of a heat engine. This was done by executing the isochoric heating and cooling strokes of an Otto cycle, respectively, in the exact- and broken-phases separated in the parameter space by an LEP. Our experimental observations are fully understood by the Lindblad master equation, which takes quantum jumps into account, and thus LEP represents a proper description of purely quantum effects involved in an Otto cycle. We have shown that the highest net work, output power, and efficiency can be achieved when the isochoric heating and cooling strokes are executed respectively in the exact phase (oscillatory dynamics and higher coherence) and broken phase (exponentially decaying dynamics and no or less coherence). This is in contrast to the conventional view that coherence in the isochoric strokes is crucial for enhanced performance of a quantum engine. This counterintuitive result would help understand thermodynamic effects in non-Hermitian systems exhibiting exceptional points and the role of quantum effects in heat-work conversion and working substance-bath interaction in heat engines. Our

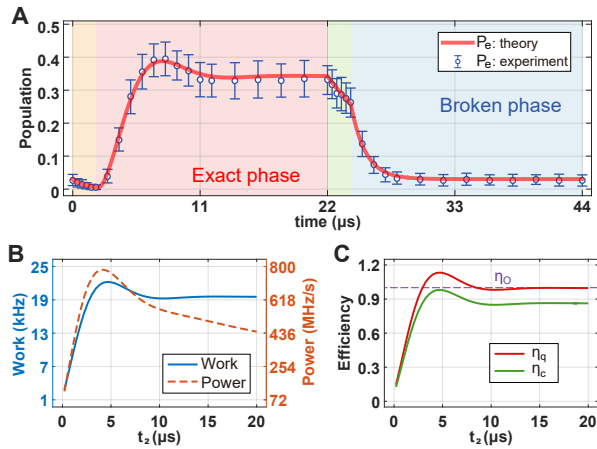


FIG. 3. The Otto cycle with the isochoric heating process in the exact phase and the isochoric cooling process in the broken phase. (A) Time evolution of the population in the excited state $|e\rangle$ when the second stroke (isochoric heating) is in the exact phase with oscillatory dynamics and the fourth stroke (isochoric cooling) is in the broken phase with non-oscillatory dynamics. The red solid curve is obtained by simulating the master equation and the circles and the error bars respectively denote the average and standard deviation of 10,000 measurements. Regions with different colors correspond to different strokes of the Otto cycle, with the orange, pink, green, and blue corresponding to the first (adiabatic compression), second (isochoric heating), third (adiabatic expansion), and fourth (isochoric cooling) strokes, respectively. The first (orange) and the third (green) strokes are implemented by up- and down-scanning the detuning Δ between $\Delta_{\min}/2\pi = 0$ kHz, and $\Delta_{\max}/2\pi = 10$ kHz, respectively, with constant Ω and γ_{eff} . The second (pink) and the fourth (blue) strokes are implemented by rapidly increasing and decreasing $\Omega/\gamma_{\text{eff}}$ with constant detuning. We used $\{\Omega/2\pi = 25$ kHz, $\gamma_{\text{eff}} = 860$ kHz $\}$, and $\{\Omega/2\pi = 25$ kHz, $\gamma_{\text{eff}} = 140$ kHz $\}$ for the first and third strokes, respectively, and $\{\Omega/2\pi = 90$ kHz, $\gamma_{\text{eff}} = 500$ kHz, $\Delta = \Delta_{\max}\}$ and $\{\Omega/2\pi = 25$ kHz, $\gamma_{\text{eff}} = 860$ kHz, $\Delta = \Delta_{\min}\}$ for the second and fourth strokes, respectively. (B), The net work and output power, and (C) the efficiencies η_c and η_q as functions of the second stroke execution time t_2 (≤ 20 μs), while the execution times of the other strokes are kept fixed. In (C), the horizontal dashed line represents the efficiency $\eta_O = 1$ of the ideal Otto cycle.

results open interesting possibilities for the control of the dynamics of quantum heat engines and will be of interest to other research areas that are concerned with the role of coherence and EPs in the enhancement of quantum processes.

Further study would evolve in two directions. First, one of the vibrational modes of the trapped ion working as the heat engine can be used as the quantum load (i.e., optical states of the ion act as the working substance and the vibrational modes coupled to them act as the load) and study heating and cooling processes in the spirit of sideband heating or sideband cooling. Second, an additional ion confined in the same trap

with the ion working as the heat engine can be used as the load. One can then rearrange the strokes of the engine cycle to perform heating or refrigeration. For example, performing the strokes of the Otto cycle in counterclockwise direction as shown in Fig. 1E with the stroke sequence as $1 \rightarrow 2 \rightarrow 3 \rightarrow 4 \rightarrow 1$ will lead to heating whereas carrying out the Otto cycle in the clockwise direction with the stroke sequence as $1 \rightarrow 4 \rightarrow 3 \rightarrow 2 \rightarrow 1$ will result in cooling. In these cases, the engine will be coupled to (decoupled from) the load during the adiabatic compression and expansion strokes (isochoric heating and cooling strokes). Performing measurements on the load after each engine cycle would then help understanding the cooling and heating process as a function of the number of engine cycles. One should however keep in mind that correlations may build up between the quantum engine and the quantum load during the adiabatic strokes (when they are coupled); therefore, one should be careful when interpreting heating/cooling, work, and other thermodynamic quantities. Further studies are needed to have a deeper physical insight into the role of Liouvillian exceptional points in the performance of quantum heat engines and to better quantify the heat, power, and efficiency of quantum heat engines coupled to quantum loads.

Data availability The data illustrated in the figures within this paper are available from the corresponding authors upon reasonable request.

Code availability The custom codes used to generate the results presented in this paper are available from the corresponding authors upon reasonable request.

* Co-first authors with equal contribution

† zhoufei@wipm.ac.cn

‡ jinghui73@foxmail.com

§ mangfeng@wipm.ac.cn

- [1] Gemmer, J., Michel, M., & Mahler, G. Quantum Thermodynamics (Springer, Berlin Heidelberg New York, 2004).
- [2] Scully, M. O., Zubairy, M. S., Agarwal, G. S., & Walther, H. Extracting Work from a Single Heat Bath via Vanishing Quantum Coherence, *Science* **299**, 862 (2003).
- [3] Parrondo, J. M. R., Horowitz, J. M. & Sagawa, T. Thermodynamics of information, *Nat. Phys.* **11**, 131 (2015).
- [4] Klatzow, J., Becker, J. N., Ledingham, P. M., Weinzetl, C., Kaczmarek, K. T., Saunders, D. J., Nunn, J., Walmsley, I. A., Uzdin, R., & Poem, E. Experimental Demonstration of Quantum Effects in the Operation of Microscopic Heat Engines, *Phys. Rev. Lett.* **122**, 110601 (2019).
- [5] Scully, M. O., Chapin, K. R., Dorfman, K. E., Kim, M. B., & Svidzinsky, A. Quantum heat engine power can be increased by noise-induced coherence, *Proc. Natl. Acad. Sci. U.S.A.* **108**, 15097 (2011).

- [6] Roßnagel, J., Abah, O., Schmidt-Kaler, F., Singer, K., & Lutz, E. Nanoscale Heat Engine Beyond the Carnot Limit, *Phys. Rev. Lett.* **112**, 030602 (2014).
- [7] Hardal, A. Ü. C. & Müstecaplıoğlu, Ö. E. Superradiant Quantum Heat Engine, *Sci Rep.* **5**, 12953 (2015).
- [8] Roßnagel, J., Dawkins, S. T., Tolazzi, K. N., Abah, O., Lutz, E., Schmidt-Kaler, F., & Singer, K. A single-atom heat engine, *Science* **352**, 325 (2016).
- [9] Maslennikov, G., Ding, S. Q., Hablutzel, R., Gan, J., Roulet, A., Nimmrichter, S., Dai, J., Scarani, V., & Matsukevich, D. Quantum absorption refrigerator with trapped ions, *Nat. Commun.* **10**, 202 (2019).
- [10] von Lindenfels, D., Gräß, O., Schmiegelow, C. T., Kaushal, V., Schulz, J., Mitchison, M. T., Goold, J., Schmidt-Kaler, F., & Poschinger, U. G. Spin Heat Engine Coupled to a Harmonic-Oscillator Flywheel, *Phys. Rev. Lett.* **123**, 080602 (2019).
- [11] Ryan, C. A., Moussa, O., Baugh, J. & Laflamme, R. Spin Based Heat Engine: Demonstration of Multiple Rounds of Algorithmic Cooling, *Phys. Rev. Lett.* **100**, 140501 (2008).
- [12] Peterson, J. P. S., Batalhão, T. B., Herrera, M., Souza, A. M., Sarthour, R. S., Oliveira, I. S., & Serra, R. M. Experimental Characterization of a Spin Quantum Heat Engine, *Phys. Rev. Lett.* **123**, 240601 (2019).
- [13] Koski, J. V., Maisi, V. F., Pekola, J. P., & Averin, D. V. Experimental realization of a Szilard engine with a single electron, *Proc. Natl. Acad. Sci. U.S.A.* **111**, 13786 (2014).
- [14] Ono, K., Shevchenko, S. N., Mori, T., Moriyama, S., & Nori, F. Analog of a Quantum Heat Engine Using a Single-Spin Qubit, *Phys. Rev. Lett.* **125**, 166802 (2020).
- [15] Quan, H. T., Wang, Y. D., Liu, Y. X., Sun, C. P., & Nori, F. Maxwell Demon Assisted Thermodynamic Cycle in Superconducting Quantum Circuits, *Phys. Rev. Lett.* **97**, 180402 (2006).
- [16] Guthrie, A., Satrya, C. D., Chang, Y.-C., Mencil, P., Nori, F., & Pekola, J. P. A Cooper-Pair Box Architecture for Cyclic Quantum Heat Engines. Preprint at <https://doi.org/10.48550/arXiv.2109.03023>.
- [17] Zhang, K., Bariani, F., & Meystre, P. Quantum optomechanical heat engine, *Phys. Rev. Lett.* **112**, 150602 (2014).
- [18] Dechant, A., Kiesel, N., & Lutz, E. All-Optical Nanomechanical Heat Engine, *Phys. Rev. Lett.* **114**, 183602 (2015).
- [19] Bender, C. M., & Boettcher, S. Real Spectra in Non-Hermitian Hamiltonians having \mathcal{PT} -Symmetry, *Phys. Rev. Lett.* **80**, 5243 (1998).
- [20] Miri, M.-A., & Alú, A. Exceptional points in optics and photonics, *Science* **363**, 42 (2019).
- [21] Özdemir, S. K., Rotter, S., Nori, F., & Yang, L. Parity-time symmetry and exceptional points in photonics, *Nat. Mater.* **18**, 783 (2019).
- [22] Pan, M. S., Zhao, H., Miao, P., Longhi, S., & Feng, L. Photonic zero mode in a non-Hermitian photonic lattice, *Nat. Commun.* **9**, 1308 (2018).
- [23] Wang, H., Lai, Y. H., Yuan, Z. Q., Suh, M. G., & Vahala, K. Petermann-factor sensitivity limit near an exceptional point in a Brillouin ring laser gyroscope, *Nat. Commun.* **11**, 1610 (2018).
- [24] El-Ganainy, R., Makris, K. G., Khajavikhan, M., Musslimani, Z. H., Rotter, S. & Christodoulides, D. N. Non-Hermitian physics and \mathcal{PT} symmetry, *Nat. Phys.* **14**, 11 (2018).
- [25] Hokmabadi, M. P., Schumer, A., Christodoulides, D. N., & Khajavikhan, M., Non-Hermitian ring laser gyroscopes with enhanced Sagnac sensitivity, *Nature (London)* **576**, 70 (2019).
- [26] Ergoktas, M. S., Soleymani, S., Kakenov, N., Wang, K., Smith, T. B., Bakan, G., Balci, S., Principi, A., Novoselov, K. S., Özdemir, S. K., & Kocabas, C. Topological engineering of terahertz light using electrically tunable exceptional point singularities, *Science* **376**, 184 (2022).
- [27] Soleymani, S., Zhong, Q., Mokim, M., Rotter, S., El-Ganainy, R. & Özdemir, S. K. Chiral and degenerate perfect absorption on exceptional surfaces, *Nat Commun* **13**, 599 (2022).
- [28] Wu, Y., Liu, W. Q., Geng, J. P., Song, X. R., Ye, X. Y., Duan, C. K., Rong, X., & Du, J. F. Observation of parity-time symmetry breaking in a single-spin system, *Science* **364**, 878 (2019).
- [29] Yu, S., Meng, Y., Tang, J. S., Xu, X. Y., Wang, Y. T., Yin, P., Ke, Z. J., Liu, W., Li, Z. P., Yang, Y. Z., Chen, G., Han, Y. J., Li, C. F., & Guo, G. C. Experimental Investigation of Quantum \mathcal{PT} -Enhanced Sensor, *Phys. Rev. Lett.* **125**, 240506 (2020).
- [30] Xiao, L., Zhan, X., Bian, Z. H., Wang, K. K., Zhang, X., Wang, X. P., Li, J., Mochizuki, K., Kim, D., Kawakami, N., Yi, W., Obuse, H., Sanders, B. C., & Xue, P. Observation of topological edge states in parity-time-symmetric quantum walks, *Nat. Phys.* **18**, 783 (2019).
- [31] Ding, L. Y., Shi, K. Y., Zhang, Q. X., Shen, D. N., Zhang, X., & Zhang, W. Experimental Determination of \mathcal{PT} -Symmetric Exceptional Points in a Single Trapped Ion, *Phys. Rev. Lett.* **126**, 083604 (2021).
- [32] Wang, W. C., Zhou, Y. L., Zhang, H. L., Zhang, J., Zhang, M. C., Xie, Y., Wu, C. W., Chen, T., Ou, B. Q., Wu, W., Jing, H., & Chen, P. X. Observation of \mathcal{PT} -symmetric quantum coherence in a single-ion system, *Phys. Rev. A* **103**, L020201 (2021).
- [33] Abbasi, M., Chen, W. J., Naghiloo, M., Joglekar, Y. N., & Murch, K. W. Topological quantum state control through Floquet exceptional-point proximity, *Phys. Rev. Lett.* **128**, 160401 (2022).
- [34] Minganti, F., Miranowicz, A., Chhajlany, R. W., & Nori, F. Quantum exceptional points of non-Hermitian Hamiltonians and Liouvillians: The effects of quantum jumps, *Phys. Rev. A* **100**, 062131 (2019).
- [35] Naghiloo, M., Abbasi, M., Joglekar, Y. N. & Murch, K. W. Quantum state tomography across the exceptional point in a single dissipative qubit. *Nat. Phys.* **15**, 1232 (2019).
- [36] Xiao, L., Wang, K., Zhan, X., Bian, Z., Kawabata, K., Ueda, M., Yi, W. & Xue, P. Observation of Critical Phenomena in Parity-Time-Symmetric Quantum Dynamics, *Phys. Rev. Lett.* **123**, 230401 (2019).
- [37] Khandelwal, S., Brunner, N., & Haack, G. Signatures of Liouvillian Exceptional Points in a Quantum Thermal Machine, *Phys. Rev. X. Quantum.* **2**, 040346 (2021).
- [38] Chen, W. J., Abbasi, M., Ha, B., Erdamar, S., Joglekar, Y. N., & Murch, K. W. Decoherence Induced Exceptional Points in a Dissipative Superconducting Qubit, *Phys. Rev. Lett.* **128**, 110402 (2022).
- [39] Chen, W. J., Abbasi, M., Joglekar, Y. N., & Murch, K. W. Quantum Jumps in the Non-Hermitian Dynamics of a Superconducting Qubit, *Phys. Rev. Lett.* **127**, 140504 (2021).

- [40] Yan, L. L., Xiong, T. P., Rehan, K., Zhou, F., Liang, D. F., Chen, L., Zhang, J. Q., Yang, W. L., Ma, Z. H., & Feng, M. Single-Atom Demonstration of the Quantum Landauer Principle, *Phys. Rev. Lett.* **120**, 210601 (2018).
- [41] Zhang, J. W., Rehan, K., Li, M., Li, J. C., Chen, L., Su, S. L., Yan, L. L., Zhou, F., & Feng, M. Single-atom verification of the information-theoretical bound of irreversibility at the quantum level, *Phys. Rev. Research* **2**, 033082 (2020).
- [42] Zhang, J. W., Yan, L. L., Li, J. C., Ding, G. Y., Bu, J. T., Chen, L., Su, S. L., Zhou, F., & Feng, M. Single-atom verification of the noise-resilient and fast characteristics of universal nonadiabatic noncyclic geometric quantum gates, *Phys. Rev. Lett.* **127**, 030502 (2021).
- [43] Huber, J., Kirton, P., Rotter, S., & Rabl, P. Emergence of \mathcal{PT} -symmetry breaking in open quantum systems, *SciPost Phys.* **9**, 52 (2020).
- [44] Nakanishi, Y., & Sasamoto, T. PT phase transition in open quantum systems with Lindblad dynamics, *Phys. Rev. A* **105**, 022219 (2022).
- [45] Quan, H. T., Liu, Y. X., Sun, C. P., & Nori, F. Quantum thermodynamic cycles and quantum heat engine, *Phys. Rev. E* **76**, 031105 (2007).
- [46] Benenti, G., Casati, G., Saito, K., & Whitney, R. S. Fundamental aspects of steady-state conversion of heat to work at the nanoscale, *Phys. Rep.* **694**, 1 (2017).
- [47] Josefsson, M., Svilans, A., Burke, A. M., Hoffmann, E. A., Fahlvik, S., Thelander, C., Leijnse, M., & Linke, H. A quantum-dot heat engine operating close to the thermodynamic efficiency limits, *Nat. Nanotech* **13**, 920 (2018).

Acknowledgments

The authors are grateful to Yunlan Zuo for her help in plotting Figure 1. This work was supported by Special Project for Research and Development in Key Areas of Guangdong Province under Grant No. 2020B0303300001, by National Natural Science Foundation of China under Grant Nos. U21A20434, 12074346, 12074390, 11835011, 11804375, 11804308, 91636220, by Postdoctoral Science Foundation of China under Grant No. 2022MT10881, by Natural Science Foundation of Henan Province under Grant No. 202300410481 and 212300410085, by K. C. Wong Education Foundation (GJTD-2019-15). S.K.O acknowledges the support from Air Force Office of Scientific Research (AFOSR) Multidisciplinary University Research Initiative (MURI) Award No. FA9550-21-1-0202. F.N is supported in part by NTT Research, JST and JSPS.

Author contributions

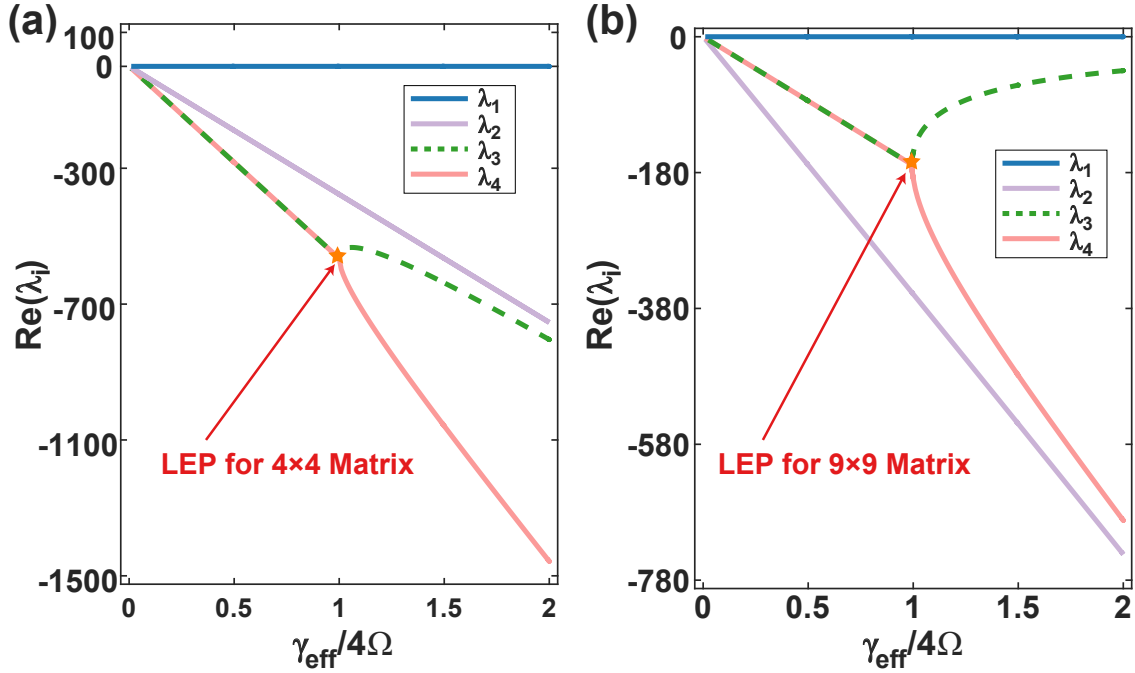
HJ and MF conceived the idea and designed the experiments; JWZ and FZ performed the experiments with help from JCL, JTB and BW. Theoretical background and simulations were provided by JQZ and GYD. All authors contributed to the discussions and the interpretations of the experimental and theoretical results. MF, HJ and SKO wrote the manuscript with inputs from all authors.

Competing interests

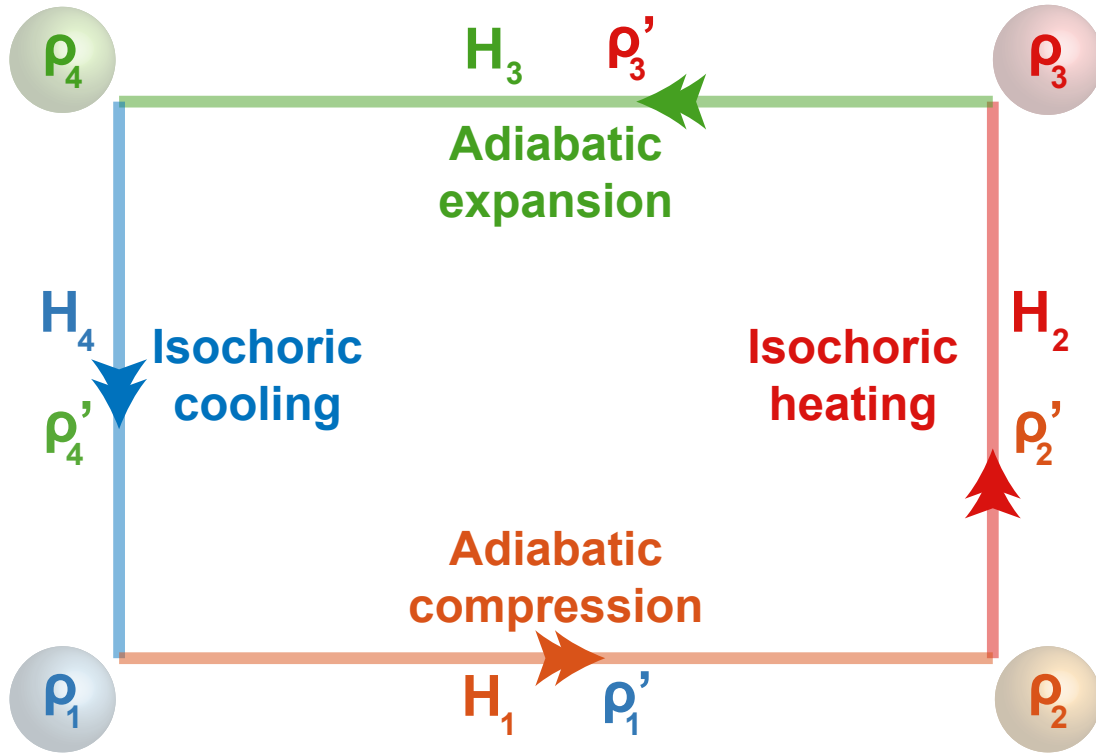
The authors declare no competing interests.

Supplementary materials for
 “Dynamic Control of Quantum Heat Engines with Exceptional Points”

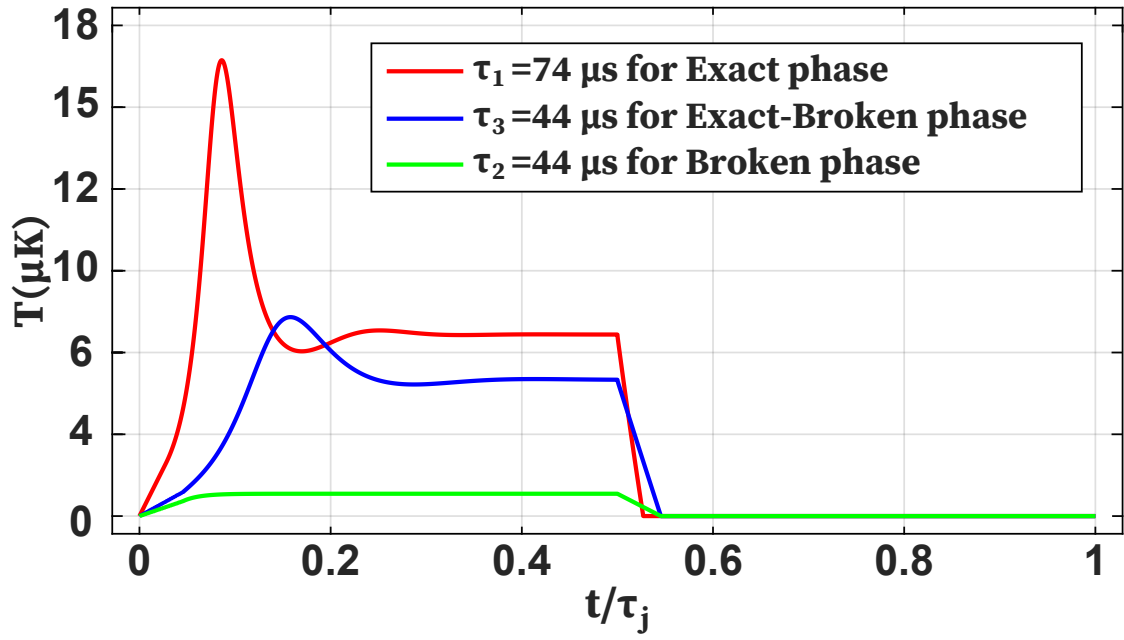
J.-W. Zhang*, J.-Q. Zhang*, G.-Y. Ding*, J.-C. Li, J.-T. Bu, B. Wang, L.-L. Yan, S.-L. Su, L. Chen, F. Nori,
 S. K. Özdemir, F. Zhou†, H. Jing‡, M. Feng§



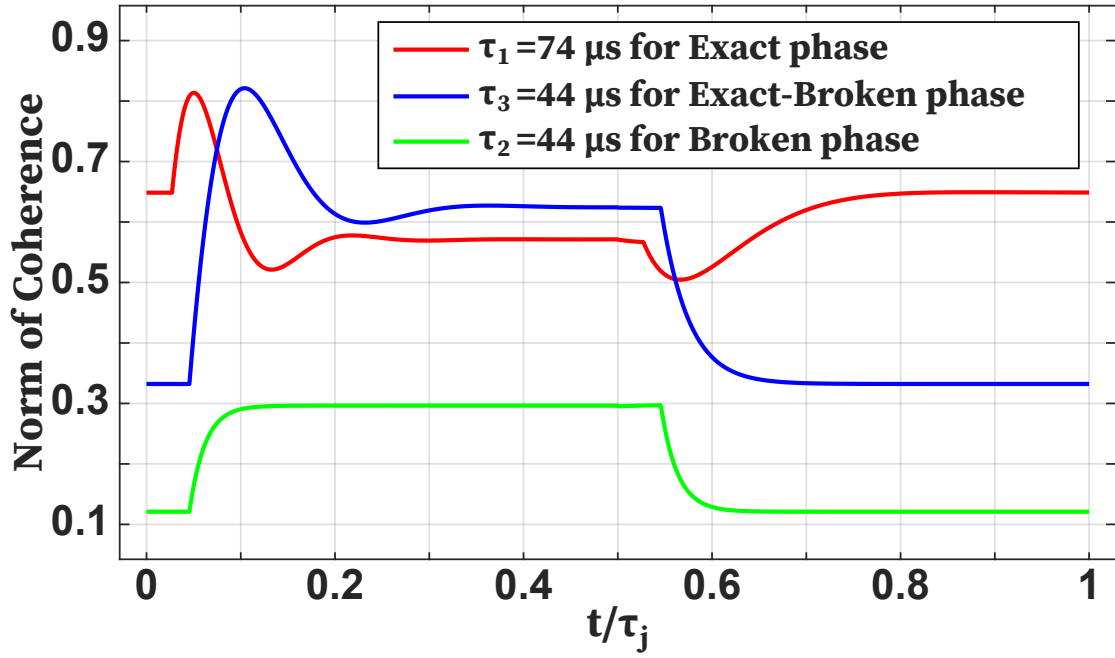
Supplementary Figure 1: Comparison of the real parts of the eigenvalues $\lambda_{3,4}$ between a 4×4 matrix (i.e., effective two-level case) and a 9×9 matrix (i.e., three-level case) with respect to $\gamma_{\text{eff}}/4\Omega$. We see the bifurcations (denoted by orange stars) in both panels occur at $\gamma_{\text{eff}}/4\Omega = 1$, indicating that the two cases share the same Liouvillian exceptional point (LEP). The horizontal blue line shows λ_1 and the pink straight line indicates λ_2 , but both are irrelevant to our experimental observation. For the case of 9×9 matrix, we only plot four eigenvalues for comparison, and neglect the remaining unphysical eigenvalues.



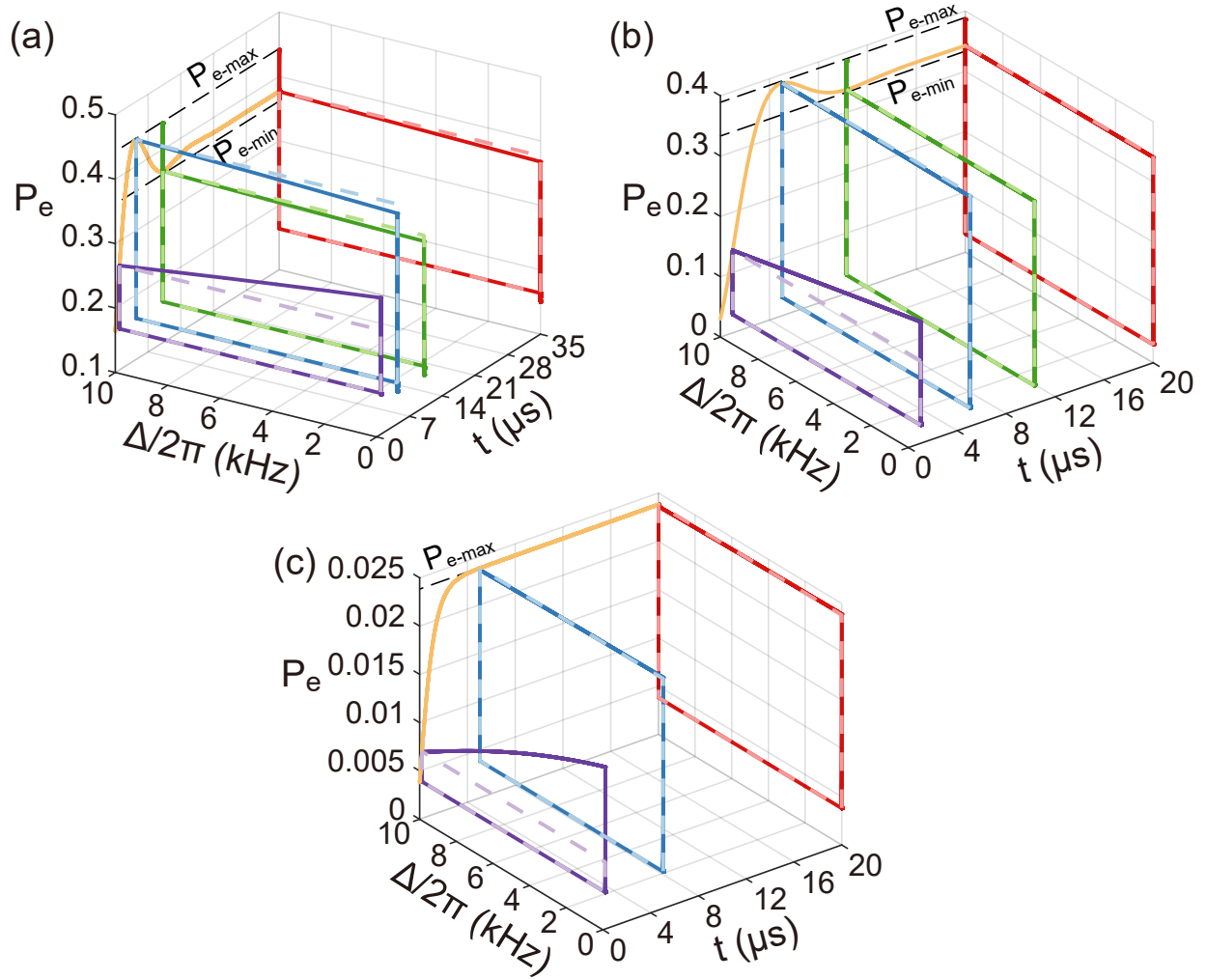
Supplementary Figure 2: A quantum Otto cycle is composed of four strokes: two adiabatic strokes referred to as adiabatic compression and expansion and two isochoric strokes describing the energy exchange with a hot and cold bath. The density operators remain constant during adiabatic strokes, that is $\rho_2 = \rho_1$, and $\rho_3 = \rho_4$. The density operators change during the isochoric strokes, implying energy exchange with either the hot or cold bath. H_i denotes the Hamiltonian describing the i th stroke, and ρ_i' represent the time-dependent matrix in the i th Stroke.



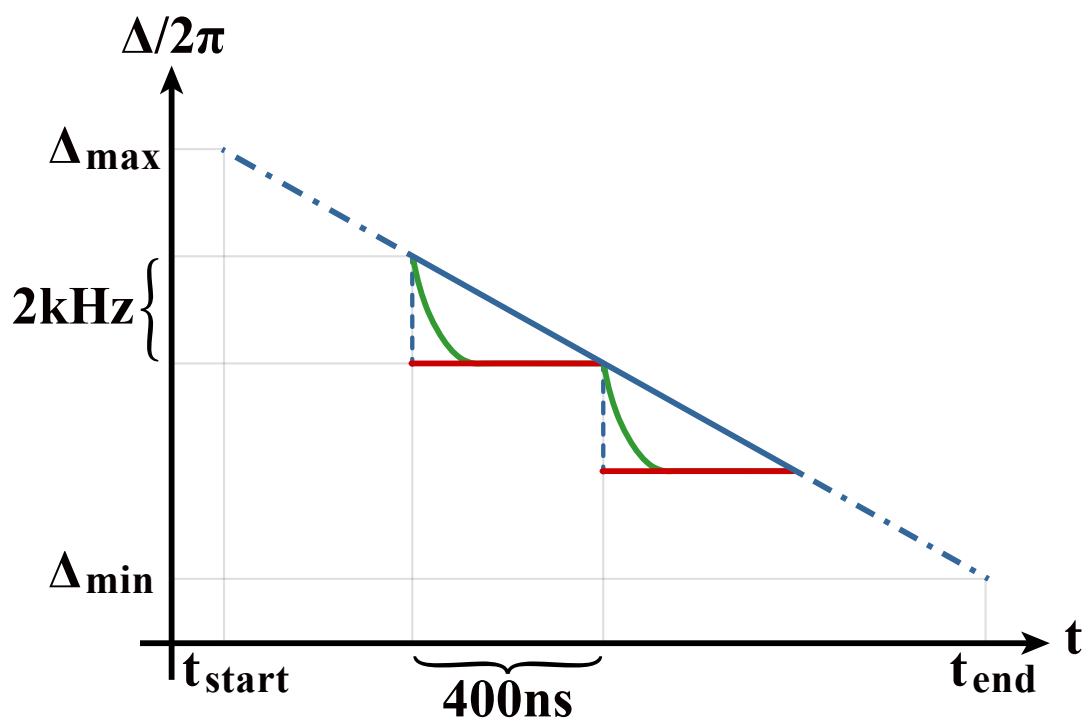
Supplementary Figure 3: Time evolution of the effective temperature T_{eff} in a quantum Otto cycle in the single ion heat engine. The red and green curves represent, respectively, the Otto cycle with both isochoric processes in the exact phase and both in the broken phase. The blue curve represents the isochoric heating process in the exact phase but the isochoric cooling process in the broken phase. τ_i is the total execution time of the Otto cycle.



Supplementary Figure 4: The evolution of coherence in a quantum Otto cycle in the trapped single ion heat engine. The red and green curves represent, respectively, the Otto cycle with both isochoric processes are implemented in the exact phase and in the broken phase. Blue curve represents the case where the isochoric heating process is implemented in the exact phase and the isochoric cooling process implemented in the broken phase. τ_i is the total execution time of the Otto cycle.



Supplementary Figure 5: Dynamical evolution of the population versus the duration of the isochoric heating stroke. (a), (b) and (c) represent, respectively, the Otto cycle with isochoric processes in exact phase, with the isochoric heating process in exact phase but the isochoric cooling process in broken phase, and with isochoric processes in broken phase. The dashed lines correspond to the ideal evolution of the population and the solid lines represent numerical simulation using experimentally available parameter values.



Supplementary Figure 6: Schematic for the sequential change of Δ in the adiabatic expansion stroke. Ideally, the detuning Δ should be tuned smoothly in a continuous fashion (blue line). In the experiments; however, this is approximated by a sequence of discrete steps where each step decreases the detuning by 2 kHz within 400 ns (red line) using an acousto-optic modulator (AOM). This results in a tuning curve (green) which is slightly different than the ideal tuning curve (blue), leading to unexpected phases in the operation of our system.

Supplementary Note 1: Hamiltonian and Effective decay rate

The Hamiltonian describing the three-level system which corresponds to the single trapped ion in our experiments is given as:

$$H_s = \omega_e |e\rangle \langle e| + \omega_p |p\rangle \langle p| + \frac{\Omega}{2} (|e\rangle \langle g| e^{-i\omega_l t} + |g\rangle \langle e| e^{i\omega_l t}) + \frac{\Omega_p}{2} (|e\rangle \langle p| e^{i\omega_d t} + |p\rangle \langle e| e^{-i\omega_d t}), \quad (\text{S1})$$

where ω_p and ω_e are, respectively, the energies of the levels $|p\rangle$ and $|e\rangle$ with respect to the level $|g\rangle$, and ω_l and ω_d are, respectively, the frequencies of the lasers coupling $|g\rangle$ to $|e\rangle$ and $|e\rangle$ to $|p\rangle$. This Hamiltonian H_s satisfies the Schrödinger equation (in units of $\hbar = 1$)

$$\frac{d}{dt} |\psi\rangle_s = -iH_s |\psi\rangle_s, \quad (\text{S2})$$

where $H_s = H_0 + H_1(t)$, with H_0 corresponding to the time-independent part of the Hamiltonian. Then defining $|\psi\rangle_s = U_I |\psi\rangle_I$ with $U_I = e^{-iH_0 t}$, we rewrite the Schrödinger equation and obtain

$$U_I^\dagger U_I \frac{d}{dt} |\psi\rangle_I = -i \left(U_I^\dagger H_s U_I - i U_I^\dagger \frac{dU_I}{dt} \right) |\psi\rangle_I = -i H_I |\psi\rangle_I, \quad (\text{S3})$$

which implies that the Hamiltonian H_I in the interaction picture satisfies

$$H_I = U_I^\dagger H_s U_I - i U_I^\dagger \frac{dU_I}{dt} = U_I^\dagger H_s U_I - H_0. \quad (\text{S4})$$

Defining $H_0 = \omega_l |e\rangle \langle e| + \omega_p |p\rangle \langle p|$ and using the Baker-Hausdorff formula

$$e^{iH_0 t} A e^{-iH_0 t} = A + it[H_0, A] + \frac{(it)^2}{2!} [H_0, [H_0, A]] + \dots \quad (\text{S5})$$

we find

$$H_I = \Delta |e\rangle \langle e| + \frac{\Omega}{2} (|e\rangle \langle g| + |g\rangle \langle e|) + \frac{\Omega_p}{2} (|e\rangle \langle p| + |p\rangle \langle e|), \quad (\text{S6})$$

where we have $\Delta = \omega_e - \omega_l$ and $\omega_p = \omega_d + \omega_l$, $\omega_d = \omega_p - \omega_l = \omega_p - (\omega_e - \Delta) \simeq \omega_p - \omega_e$. The effective Hamiltonian H_{eff} is then given by [S1]

$$H_{\text{eff}} = -\frac{1}{2} V_- [H_{\text{NH}}^{-1} + (H_{\text{NH}}^{-1})^\dagger] V_+ = \Delta |e\rangle \langle e| + \frac{\Omega}{2} (|e\rangle \langle g| + |g\rangle \langle e|), \quad (\text{S7})$$

where the non-Hermitian Hamiltonian H_{NH} is given by $H_{\text{NH}} = -\frac{i}{2} (\gamma_e + \gamma_g) |p\rangle \langle p| = -\frac{i}{2} \gamma |p\rangle \langle p|$, with γ_i corresponding to the decay rate from the level $|p\rangle$ to the level $|i\rangle$, while the perturbative excitations V_+ and de-excitations V_- are defined as $V_+ = \frac{\Omega_p}{2} |p\rangle \langle e| + \frac{\Omega}{2} |e\rangle \langle g|$ and $V_- = \frac{\Omega_p}{2} |e\rangle \langle p| + \frac{\Omega}{2} |g\rangle \langle e|$. We then write the effective Lindblad operator as [S1]

$$L_{\text{eff}}^{e \rightarrow g} = i\sqrt{\gamma_g} \frac{\Omega_p}{\gamma} |g\rangle \langle e|, \quad (\text{S8})$$

from which the effective decay rate γ_{eff} from the excited state $|e\rangle$ to the ground state $|g\rangle$ is found as

$$\gamma_{\text{eff}} = \frac{\gamma_g \Omega_p^2}{\gamma^2} = \frac{(\gamma - \gamma_e) \Omega_p^2}{\gamma^2} = \left(1 - \frac{\gamma_e}{\gamma}\right) \frac{\Omega_p^2}{\gamma} \simeq \frac{\Omega_p^2}{\gamma}. \quad (\text{S9})$$

The same result by an alternative method can be found in [S2]. We note that the expression for H_{eff} in Eq. (S7) is the same as Eq. (2) in the main text and γ_{eff} appears in Eq. (1) of the main text and in the expression of the LEP of the system.

Supplementary Note 2: Liouvillian Exceptional Points

Our system obeys the Lindblad master equation $\dot{\rho}(t) = \mathcal{L}\rho(t)$ as defined in Eq. (1) of the main text. Here

\mathcal{L} is the Liouvillian superoperator and ρ is the density operator of the system. From the Hamiltonian, as written in Eq. (S7) and Eq. (2) of the main text, we can write \mathcal{L} as

$$\mathcal{L} = \begin{pmatrix} -\gamma_{\text{eff}} & i\Omega/2 & -i\Omega/2 & 0 \\ i\Omega/2 & -(\gamma_{\text{eff}}/2 + i\Delta) & 0 & -i\Omega/2 \\ -i\Omega/2 & 0 & -(\gamma_{\text{eff}}/2 - i\Delta) & i\Omega/2 \\ \gamma_{\text{eff}} & -i\Omega/2 & i\Omega/2 & 0 \end{pmatrix}$$

By setting $\Delta = 0$, we find the eigenvalues of \mathcal{L} as $\lambda_1 = 0$, $\lambda_2 = -\gamma_{\text{eff}}$, $\lambda_3 = \frac{1}{4}(-3\gamma_{\text{eff}} - \sqrt{\gamma_{\text{eff}}^2 - 16\Omega^2})$, and $\lambda_4 = \frac{1}{4}(-3\gamma_{\text{eff}} + \sqrt{\gamma_{\text{eff}}^2 - 16\Omega^2})$.

Since these eigenvalues are related to dissipation terms, their real parts indicate decaying effects while their imaginary parts define the eigenenergies [S3]. It is easily seen that the eigenvalues λ_3 and λ_4 become degenerate and an LEP emerges at $\lambda_3 = \lambda_4 = -3\gamma_{\text{eff}}/4$, when $\gamma_{\text{eff}} = 4\Omega$. As explained in the main text, for $\gamma_{\text{eff}} > 4\Omega$, we have real λ_3 and λ_4 with a splitting amount given by $\xi = \sqrt{\gamma_{\text{eff}}^2 - 16\Omega^2}$. Thus, when $\gamma_{\text{eff}} > 4\Omega$, the system is in the broken phase. For $\gamma_{\text{eff}} < 4\Omega$, on the other hand, λ_3 and λ_4 become complex conjugate pairs with a splitting of ξ in their imaginary parts, corresponding to the exact phase.

Moreover, to justify the validity of our reduced matrix, i.e., Eq. (12), which comes from the effective Hamiltonian Eq. (8), we have calculated the LEPs for both Hamiltonians (S6) and (S7), and found that the LEPs share the same decay rate as written in (S9) in the case of $\Delta = 0$. This is further confirmed in Supplementary Figure 1. The eigenvectors corresponding to the above eigenvalues are,

$$\rho_1 = \begin{pmatrix} \frac{\Omega^2}{\gamma_{\text{eff}}^2 + \Omega^2} & -i\frac{\gamma_{\text{eff}}\Omega}{\gamma_{\text{eff}}^2 + \Omega^2} \\ i\frac{\gamma_{\text{eff}}\Omega}{\gamma_{\text{eff}}^2 + \Omega^2} & 0 \end{pmatrix}, \quad \rho_2 = \begin{pmatrix} 0 & 1 \\ 1 & 0 \end{pmatrix}, \quad (\text{S10})$$

and

$$\rho_{3,4} = \begin{pmatrix} -1 & -\frac{-i\gamma_{\text{eff}} \pm \sqrt{16\Omega^2 - \gamma_{\text{eff}}^2}}{4\Omega} \\ \frac{-i\gamma_{\text{eff}} \pm \sqrt{16\Omega^2 - \gamma_{\text{eff}}^2}}{4\Omega} & 1 \end{pmatrix}, \quad (\text{S11})$$

Clearly, at $\Delta = 0$ and $\gamma_{\text{eff}} = 4\Omega$, the eigenstates ρ_3 and ρ_4 coalesce, confirming that a second-order LEP emerges at $\gamma_{\text{eff}} = 4\Omega$, separating the exact- and broken-phases.

Supplementary Note 3: Thermodynamic quantities

In this section, we present the definitions and discussions on the five thermodynamic quantities [S4]: the net work W , the output power P , and the efficiencies η_o , η_c , η_q . We note that in our system of a trapped ion, the internal energy of the spin heat engine is defined as $U = \text{tr}(\rho H)$, where ρ and H are the density matrix and Hamiltonian of the spin system, respectively. Moreover, the Hamiltonian $H = \Delta |e\rangle\langle e|$, the coupling strength Ω , and the effective dissipation rate γ_{eff} are used to tune the system such that an Otto engine cycle is performed, as explained in the main text. Quantum coherence affecting the performance of the quantum Otto cycles in our system is investigated by tuning the execution time t_2 .

The net work and output power

In classical thermodynamics, the first law of thermodynamics is expressed as $dU = dW + dQ$. In contrast, in quantum thermodynamics [S4, S5], it is expressed as $dU = d(\text{tr}(\rho H)) = \text{tr}(\rho dH) + \text{tr}(H d\rho)$ where the work and heat in differential form are defined as $dW = \rho dH$ and $dQ = H d\rho$, respectively. Then the energy absorption Q_{in} from the hot bath and the energy dissipation Q_{out} to the cold bath can be written as $Q_{\text{in}} = \sum_i H_i d\rho'_i$ (for $d\rho'_i > 0$) and $Q_{\text{out}} = \sum_i H_i d\rho'_i$ (for $d\rho'_i < 0$), respectively (see Supplementary Figure 2). As we discussed in the main text, when Q_{in} and Q_{out} are calculated for our quantum Otto cycle, we see that during both of the isochoric processes the system absorbs and releases energy due to the quantum coherence involved. This is reflected in the oscillation observed in the populations of the excited and ground states. Thus, the net acquired work and the corresponding

output power can be written, respectively, as

$$W = Q_{\text{in}} + Q_{\text{out}} = \sum_i H_i d\rho'_i, \quad (\text{S12})$$

and

$$P = W/(t_1 + t_2 + t_3 + t_4), \quad (\text{S13})$$

where t_i is the execution time of the i -th Stroke in the cycle.

Heat engine efficiencies

Ideal Otto engine efficiency η_o : In an ideal adiabatic process, the density matrix remains constant ($\rho_2 = \rho_1$, and $\rho_3 = \rho_4$), where ρ_2 and ρ_3 are the density matrices of the initial and final states of the isochoric heating process, respectively, and ρ_4 and ρ_1 are the density operators in the isochoric cooling process (See main text Fig. 1F).

In classical thermodynamics, the energy can be transferred only from a hot system to a cold one, and the energy flow is unidirectional. We can write the energy absorption from the hot bath during the isochoric heating stroke as

$$Q_{\text{in}}^o = \text{tr}[(\rho_3 - \rho_2)H_2], \quad (\text{S14})$$

and the energy release to the cold bath during the isochoric cooling stroke as

$$Q_{\text{out}}^o = \text{tr}[(\rho_4 - \rho_1)H_4], \quad (\text{S15})$$

where $H_2 = \Delta_{\text{max}} |e\rangle \langle e|$ and $H_4 = \Delta_{\text{min}} |e\rangle \langle e|$ are the Hamiltonians in the isochoric heating and cooling strokes, respectively. Here, Δ_{min} and Δ_{max} are the minimum and maximum detunings, respectively. So, the corresponding ideal Otto engine efficiency can be written as

$$\eta_o = 1 - \frac{Q_{\text{out}}^o}{Q_{\text{in}}^o} = 1 - \frac{\Delta_{\text{min}}}{\Delta_{\text{max}}}, \quad (\text{S16})$$

which is in the ideal limit ($\eta_o = 1$) when $\Delta_{\text{min}} = 0$.

Conventional Otto engine efficiency η_c : The efficiency of the conventional Otto cycle is defined by

$$\eta_c = \frac{W}{Q_{\text{in}}} = 1 - \frac{Q_{\text{out}}}{Q_{\text{in}}}. \quad (\text{S17})$$

Quantum Otto engine efficiency η_q : In contrast to the classical counterpart, the heat absorption takes place during both the isochoric heating and cooling strokes of a quantum Otto cycle. To focus on the coherent effects in the isochoric heating process, we define η_q to be only regarding the heat absorption in the isochoric heating process:

$$\eta_q = \frac{W}{Q_{\text{in}}^q}, \quad (\text{S18})$$

where $W = H_2 d\rho'_2 + H_4 d\rho'_4 = \text{tr}[H_2(\rho_3 - \rho_2)] + \text{tr}[(H_4(\rho_1 - \rho_4))]$ is the work done and Q_{in}^q is the heat absorption

$$Q_{\text{in}}^q = (P_h^L - P_h^S)\Delta_{\text{max}}, \quad (\text{S19})$$

with P_h^L and P_h^S denoting, respectively, the final steady state and initial populations in the isochoric heating process. Since there is no change in the state of the system during the adiabatic strokes, we have $\rho_1 = \rho_2 = \rho_h^S$, $\rho_3 = \rho_4 = \rho_h(t)$. Using this in the above expressions, we find η_q as

$$\eta_q = \frac{W(t)}{Q_{\text{in}}^q} = \frac{(\Delta P_e + P_h^L - P_h^S)(\Delta_{\text{max}} - \Delta_{\text{min}})}{(P_h^L - P_h^S)\Delta_{\text{max}}} = \frac{(\Delta P_e + P_h^L - P_h^S)}{(P_h^L - P_h^S)} \left(1 - \frac{\Delta_{\text{min}}}{\Delta_{\text{max}}}\right) = \left(1 + \frac{\Delta P_e}{(P_h^L - P_h^S)}\right) \eta_o, \quad (\text{S20})$$

where we have defined the time-dependent population difference caused by the quantum coherence as $\Delta P_e = P_h(t) - P_h^L$. It is clear in Eq. (S20) that η_q equals to the classical ideal Otto engine efficiency η_o , that is $\eta_q = \eta_o$ when $\Delta P_e = 0$. Similarly, we have $\eta_q > \eta_o$ for $\Delta P_e > 0$, and $\eta_q < \eta_o$ for $\Delta P_e < 0$. Since ΔP_e is a

signature of the coherence in the system, we conclude that coherence may increase or decrease the efficiency of a quantum Otto cycle.

Supplementary Note 4: Effective temperature and Coherence

In the interaction picture, we consider the two-level system consisting of the ground state $|g\rangle$ and the excited state $|e\rangle$, with energy gap Δ . The occupation probabilities P_e and P_g obey the Boltzman distribution $P_e/P_g = \exp[-\beta\Delta(t)]$, and $P_e + P_g = 1$, giving the effective temperature [S4, S5]

$$T_{\text{eff}} = \frac{1}{k_B\beta} = \frac{\Delta}{k_B} \left(\ln \frac{P_g}{P_e} \right)^{-1}. \quad (\text{S21})$$

Supplementary Figure 3 depicts the evolution of the effective temperature during a quantum Otto cycle. Here the changes in the temperature are mainly due to the detuning variation in the adiabatic compression and expansion strokes and the population oscillation in the isochoric strokes. The effective temperature can be made zero if the detuning is set to zero.

Using the expression $C_{l_1}(\rho) = \sum_{i \neq j} |\rho_{i,j}|$ for the coherence [S6], we have calculated the coherence involved in an Otto cycle in our system and presented the results in Supplementary Figure 4. We see that the coherence remaining at the end of an Otto cycle is the lowest when the system is operated such that both of the isochoric strokes are in the broken phase and the highest when both of the isochoric strokes are implemented in the exact phase.

Supplementary Note 5: Dynamical evolution of the population

We represent the dynamic evolution of the population in Supplementary Figure 5, in which more cycles are plotted for the three cases considered in our experiment, i.e., both the isochoric processes in the exact phase, the isochoric heating process in the exact phase but the isochoric cooling process in the broken phase, and both the isochoric processes in the broken phase. This figure helps to understand the variation of some key quantities in the heat engine performance.

Supplementary Note 6: Experimental details

During the implementation of the Otto cycles, we drive the qubit by an ultra-stable narrow linewidth laser with wavelength 729-nm as expressed in Eq. (2) of the main text. This driving laser is controlled by a double-pass acousto-optic modulator which helps control the phase and the frequency of the 729-nm laser. We use a field programable gate array to control a direct digital synthesizer as the frequency source of the acousto-optic modulator. We repeat each single-qubit measurement 10,000 times to minimise the quantum projection noise. Due to the noises caused by the fluctuations in the applied magnetic and electric fields, the qubit in our system suffers from dephasing of 0.81(11) kHz. Other sources of error in our experiments are the laser instability and imperfections in the single-qubit pulses, whose effects are assessed from the Rabi oscillations. After calibration, we estimate the total error in the initial-state preparation and the final-state detection to be 0.7(2)% and 0.22(8)%, respectively. The influence of these noises and imperfections are reflected in the error bars shown in the figures of the main text.

In Figs 2A₁, 2B₁ and 3A, we note a slight reduction (≈ 0.1) in the population of the excited state $|e\rangle$ during the first and third strokes. This deviation from the ideal theoretical expectation (i.e., no population change during the adiabatic compression and expansion strokes) can be attributed to the fact that in the experiments the frequency of the 729 nm laser was not tuned smoothly in a continuous fashion but instead we used a sequence of discrete steps using an AOM. As shown in Supplementary Figure 6, although the required continuous change of the detuning Δ (blue line) can be equivalently accomplished by discrete steps of operation, as plotted by the red line. In our experiments, the variation of detuning is accomplished by a sequence of AOM which leads to a slightly different tuning curve (green) due to the switching time of the AOM. This leads to imperfect variation of the detuning, bringing in unexpected phases in the operation. Nevertheless, considering these unexpected phases in numerical simulation, we have fitted the experimental observations involving such cases by theory very well, see Figs. 2A₁, 2B₁ and 3A in the main text.

* Co-first authors with equal contribution

† zhoufei@wipm.ac.cn

‡ jinghui73@foxmail.com

§ mangfeng@wipm.ac.cn

- [S1] Reiter, F., & Sørensen, A. S. Effective operator formalism for open quantum systems, *Phys. Rev. A* **85**, 032111 (2019).
- [S2] Zhang, J. W., Rehan, K., Li, M., Li, J. C., Chen, L., Su, S. L., Yan, L. L., Zhou, F., & Feng, M. Single-atom verification of the information-theoretical bound of irreversibility at the quantum level, *Phys. Rev. Research* **2**, 033082 (2020).
- [S3] Minganti, F., Miranowicz, A., Chhajlany, R. W., & Nori, F. Quantum exceptional points of non-Hermitian Hamiltonians and Liouvillians: The effects of quantum jumps, *Phys. Rev. A* **100**, 062131 (2019).
- [S4] Quan, H. T., Liu, Y. X., Sun, C. P., & Nori, F. Quantum thermodynamic cycles and quantum heat engine, *Phys. Rev. E* **76** 031105 (2007).
- [S5] Benenti, G., Casati, G., Saito, K., & Whitney, R. S. Fundamental aspects of steady-state conversion of heat to work at the nanoscale, *Phys. Rep.* **694**, 1 (2017).
- [S6] Baumgratz, T., Cramer, M., & Plenio, M. B. Quantifying Coherence, *Phys. Rev. Lett.* **113**, 140401 (2014).